

# Modal, Spectral, and Polarization Entanglement in Guided-Wave Parametric Down-Conversion

Mohammed F. Saleh,<sup>1,\*</sup> Bahaa E. A. Saleh,<sup>1,2</sup> and Malvin Carl Teich<sup>1,3</sup>

<sup>1</sup>*Quantum Photonics Laboratory, Department of Electrical and Computer Engineering, Boston University, Boston, MA 02215*

<sup>2</sup>*Quantum Photonics Laboratory, College of Optics and Photonics (CREOL),  
University of Central Florida, Orlando, FL 32816*

<sup>3</sup>*Department of Physics, Boston University, Boston, MA 02215*

(Dated: October 11, 2021)

We examine the modal, spectral, and polarization entanglement properties of photon pairs generated in a nonlinear, periodically poled, two-mode waveguide (1-D planar or 2-D circular) via nondegenerate spontaneous parametric down-conversion. Any of the possible degrees of freedom — mode number, frequency, or polarization — can be used to distinguish the down-converted photons while the others serve as attributes of entanglement. Distinguishing the down-converted photons based on their mode numbers enables us to efficiently generate spectral or polarization entanglement that is either narrowband or broadband. On the other hand, when the generated photons are distinguished by their frequencies in a Type-0 process, modal entanglement turns out to be an efficient alternative to polarization entanglement. Moreover, modal entanglement in Type-II down-conversion may be used to generate a doubly entangled state in frequency and polarization.

PACS numbers: 42.65.Wi, 42.65.Lm, 42.50.Dv

## I. INTRODUCTION

Photon pairs generated via the nonlinear process of spontaneous parametric down-conversion (SPDC) can exhibit entanglement in multiple degrees of freedom: spectral, spatial, and polarization [1]. Entanglement arises from the multiple possibilities for satisfying energy and momentum conservation, as required by the parametric interaction process. Spectral entanglement is exhibited equivalently in time or energy [2]; spatial entanglement may be manifested as entanglement in wavevector direction [3], transverse direction [4], orbital-angular-momentum (OAM) [5], or spatial parity [6, 7]. A proper description of the quantum state of the photon pair (biphoton) requires a Hilbert space that includes all of the pertinent degrees of freedom. One of these degrees of freedom may be arbitrarily chosen to distinguish the two photons, while the other two are used to describe the state. The term hyper-entanglement has been used to describe states defined over multiple degrees of freedom [8].

While the polarization variable is intrinsically binary, spectral and spatial variables are generally continuous. Nevertheless, binary spectral or spatial degrees of freedom can be extracted by selection of a subspace of dimension two (a qubit). Examples are frequency selection by use of narrow spectral filters [9], direction selection by use of pinholes in the far field [10], and lower-order OAM-mode selection by suppression of higher-order modes [11]. Another approach to binarization is based on constraining the parametric process in such a way that only two values of the continuous variable are permitted; such

configurations include narrowband spectral entanglement [12] and Type-II noncollinear down-conversion in which only two directions (as determined by intersecting rings) are permitted [13]. A third approach is to map the larger Hilbert space onto a binary space, as in spatial-parity entanglement [6, 14].

In this paper, we consider the generation of biphotons by means of SPDC in a nonlinear waveguide. This configuration confines the photons to a single direction of propagation and discretizes the spatial degree of freedom to the waveguide spatial modes. For a two-mode waveguide, the spatial degree of freedom is binary, representing a modal qubit. The waveguide also supports two polarizations (e.g., TE and TM in a one-dimensional geometry). Moreover, the spectral distributions of the down-converted photons may be constrained to yield a pair of narrow spectral lines defining a spectral qubit, or alternatively, may be made more flexible so as to generate photon pairs with broad spectral entanglement; these conditions are achieved by making use of periodic and linearly chirped poling of the nonlinear medium, respectively.

In addition to the advantage of spatial binarization, the two-mode waveguide has the merit of combining a higher rate of biphoton generation, normally obtained in collinear degenerate bulk SPDC, with the photon separability generally offered by a noncollinear configuration. Moreover, processing of the generated biphotons for applications in quantum information [15] is often facilitated by the use of guided-wave devices.

In this paper, we offer a comprehensive theoretical study of the properties and applications of modal, spectral, and polarization entanglement of biphotons generated via SPDC in 1-D planar and 2-D circular waveguides. In particular, we consider biphotons generated via different types of interactions and with the use of a

---

\*Electronic address: mohsaleh@bu.edu

continuous wave (CW) pump. Prior work in this area has been limited and has made use of a pulsed, rather than CW, pump [16, 17].

The paper is organized as follows. In Sec. II, we develop a general theory for SPDC in periodically poled multimode waveguides. In Sec. III, we determine the waveguide parameters required to generate modal and spectral or polarization entanglement in 1-D planar waveguides using either Type-0 or Type-II interactions. A similar study is carried out in Sec. IV for 2-D circular waveguides (optical fibers). Features and applications of modal entanglement are considered in Sec. V. Finally, the conclusions are presented in Sec. VI.

## II. SPONTANEOUS PARAMETRIC DOWN-CONVERSION IN MULTIMODE WAVEGUIDES

Consider an SPDC process in a multimode waveguide, where a pump wave  $p$  is down-converted into a signal wave  $s$  and an idler wave  $i$ . Using time-dependent perturbation theory, the two-photon state  $|\Psi\rangle$  can be written as [12]

$$|\Psi\rangle \sim \iint d\mathbf{r} dt \mathbf{d}(\mathbf{r}) \mathbf{E}_p(\mathbf{r}, t) \hat{\mathbf{E}}_s^{(-)}(\mathbf{r}, t) \hat{\mathbf{E}}_i^{(-)}(\mathbf{r}, t) |0, 0\rangle, \quad (1)$$

where  $\mathbf{d}(\mathbf{r})$  is the second-order nonlinear-coefficient tensor;  $\mathbf{E}_p$  is the pump electric field at position  $\mathbf{r}$  and time  $t$ , treated classically and assumed to be undepleted;  $\hat{\mathbf{E}}_q^{(-)}$  are the negative-frequency parts of the signal and idler electric-field operators ( $q = s, i$ ) at position  $\mathbf{r}$  and time  $t$ ; and  $|0, 0\rangle$  is the vacuum state of the signal and the idler.

For guided waves propagating along the  $x$  direction, the electric-field operator of the signal and idler is written as

$$\hat{\mathbf{E}}_q^{(-)}(\mathbf{r}, t) = \int d\omega_q \sum_{m_q, \sigma_q} \hat{a}_{m_q, \sigma_q}^\dagger(\omega_q) u_{m_q, \sigma_q}(\omega_q, y, z) \times \exp[j\omega_q t - j\beta_{m_q, \sigma_q}(\omega_q) x], \quad (2)$$

where  $\omega_q$  is the angular frequency;  $\sigma_q$  and  $m_q$  are the polarization and spatial-mode indexes, respectively;  $\beta_{m_q, \sigma_q}$  is the propagation constant;  $u_{m_q, \sigma_q}$  is the transverse field profile in the  $y$ - $z$  plane; and  $\hat{a}_{m_q, \sigma_q}^\dagger$  is the creation operator for the wave  $q$ . For the classical pump electric field, a similar expression can be obtained by taking the complex conjugate of Eq. (2) then replacing the creation operator with the wave amplitude.

Substituting Eq. (2) into Eq. (1), assuming that  $\mathbf{d}(\mathbf{r})$  depends only on  $x$ , and noting that the integration over  $t$  yields the delta function  $\delta(\omega_p - \omega_s - \omega_i)$ , the two-photon state becomes

$$|\Psi\rangle \sim \int d\omega_s \sum_{\mathbf{m}, \sigma} \Phi_{\mathbf{m}, \sigma}(\omega_s) |\omega_s, m_s, \sigma_s\rangle |\omega_i, m_i, \sigma_i\rangle, \quad (3)$$

where

$$\Phi_{\mathbf{m}, \sigma}(\omega_s) = A_{\mathbf{m}, \sigma}(\omega_s) \int dx \mathbf{d}(x) \exp[j\Delta\beta_{\mathbf{m}, \sigma}(\omega_s) x], \quad (4)$$

$$A_{\mathbf{m}, \sigma}(\omega_s) = \iint dy dz \prod_{q=p, s, i} u_{m_q, \sigma_q}(\omega_q, y, z), \quad (5)$$

$\omega_i = \omega_p - \omega_s$ ,  $\mathbf{m} = (m_s, m_i)$ ,  $\sigma = (\sigma_s, \sigma_i)$ , and  $\Delta\beta_{\mathbf{m}, \sigma}(\omega_s) = \beta_{m_p, \sigma_p}(\omega_p) - \beta_{m_s, \sigma_s}(\omega_s) - \beta_{m_i, \sigma_i}(\omega_i)$  is the phase mismatch. The factor  $A_{\mathbf{m}, \sigma}$  represents the spatial overlap of the transverse profiles of the interacting modes. The square-magnitude of  $\Phi_{\mathbf{m}, \sigma}(\omega_s)$  represents the SPDC spectrum when the signal and the idler mode numbers are  $\mathbf{m} = (m_s, m_i)$  and their polarization indexes are  $\sigma = (\sigma_s, \sigma_i)$ .

Since the generated photons are collinear, their directions cannot be used to distinguish the two photons. If the mode number is used in this capacity, then the two-photon state described in Eq. (3) may be written as

$$|\Psi\rangle \sim \int d\omega_s \sum_{\mathbf{m}, \sigma} \Phi_{\mathbf{m}, \sigma}(\omega_s) |\omega_s, \sigma_s\rangle_{m_s} |\omega_i, \sigma_i\rangle_{m_i}. \quad (6)$$

Alternatively, using frequency as the identifier, the two-photon state takes the form

$$|\Psi\rangle \sim \int d\omega_s \sum_{\mathbf{m}, \sigma} \Phi_{\mathbf{m}, \sigma}(\omega_s) |m_s, \sigma_s\rangle_{\omega_s} |m_i, \sigma_i\rangle_{\omega_i}. \quad (7)$$

We may also use polarization as the identifier and write a similar expression for the two-photon state. These expressions for the state are, of course, equivalent.

We now derive expressions for the spectral function  $\Phi_{\mathbf{m}, \sigma}$  for quasi-phase matched (QPM) structures. Such structures are designed to phase match a specific type of interaction (Type 0 or I or II) via a certain component of the second-order nonlinear tensor; hence  $\mathbf{d}$  can be replaced by its effective value  $d_{\text{eff}}$ . Using electric poling, the nonlinear coefficient is made to alternate between  $\pm d_{\text{eff}}$  along one of the crystal principle axes, say  $x$ . The poling period can be either uniform or variable. We consider these two cases in turn.

**Uniform Poling.** For uniform poling with period  $\Lambda_0$ , the spatial distribution of the nonlinear coefficient can be represented as a sum of distinct Fourier components,  $d_{\text{eff}}(x) = \sum_{\kappa=1}^{\infty} \tilde{d}_{\kappa} \exp[-j \int_0^x dx K_{\kappa}(x)]$ , where  $\tilde{d}_{\kappa} = (2/\pi\kappa) |d_{\text{eff}}|$  and  $K_{\kappa}(x) = (2\pi\kappa/\Lambda_0)$  represent the amplitude and spatial frequency of the  $\kappa$ th Fourier component, respectively. Only that Fourier component whose phase is close to, or equal to, the phase mismatch  $\Delta\beta_{\mathbf{m}, \sigma}(\omega_s)$  will contribute to  $\Phi_{\mathbf{m}, \sigma}(\omega_s)$ . Carrying out the integration in Eq. (4) for a waveguide of length  $L$ , we obtain

$$\Phi_{\mathbf{m}, \sigma}(\omega_s) = A'_{\mathbf{m}, \sigma}(\omega_s) \text{sinc} \left[ \Delta\tilde{\beta}_{\mathbf{m}, \sigma}(\omega_s) L/2\pi \right] \times \exp \left[ j \Delta\tilde{\beta}_{\mathbf{m}, \sigma}(\omega_s) L/2 \right], \quad (8)$$

where

$$\Delta\tilde{\beta}_{\mathbf{m},\sigma}(\omega_s) = \Delta\beta_{\mathbf{m},\sigma}(\omega_s) - \frac{2\pi\kappa}{\Lambda_0}, \quad (9)$$

$A'_{\mathbf{m},\sigma}(\omega_s) = (2L/\pi\kappa)|d_{\text{eff}}|A_{\mathbf{m},\sigma}(\omega_s)$ , and  $\text{sinc}(\theta) = \sin(\pi\theta)/(\pi\theta)$ . From a practical perspective, the poling period is determined by satisfying the quasi-phase-matching condition at a certain frequency  $\omega_s$ , i.e.,  $\Delta\tilde{\beta}_{\mathbf{m},\sigma}(\omega_s) = 0$ , or  $\Delta\beta_{\mathbf{m},\sigma}(\omega_s) = 2\pi\kappa/\Lambda_0$ .

**Linearly Chirped Poling.** For linearly chirped poling with a slowly varying spatial frequency, we can still make use of a Fourier series to represent the spatial distribution of the nonlinear coefficient with  $K_\kappa(x) = 2\pi\kappa/\Lambda(x) = 2\pi\kappa/\Lambda_0 - \zeta x$ , where  $\zeta$  is the chirp parameter [18]. It is clear that it is the spatial frequency, rather than the spatial period, that is chirped. In this case, Eq. (4) yields

$$\Phi_{\mathbf{m},\sigma}(\omega_s) = A''_{\mathbf{m},\sigma}(\omega_s) \exp\left[\frac{-j\Delta\tilde{\beta}_{\mathbf{m},\sigma}^2(\omega_s)}{2\zeta}\right] \times [\gamma(L) - \gamma(0)], \quad (10)$$

where  $A''_{\mathbf{m},\sigma}(\omega_s) = |d_{\text{eff}}|A_{\mathbf{m},\sigma}(\omega_s)\sqrt{2j/\pi\zeta\kappa^2}$ ,  $\gamma(x) = \text{erfi}\{[\Delta\tilde{\beta}_{\mathbf{m},\sigma}(\omega_s) + \zeta x]/\sqrt{-2j\zeta}\}$ ,  $\text{erfi}(\theta) = -j\text{erf}(j\theta)$  and  $\text{erf}(\cdot)$  is the error function. In the remainder of this paper, we use  $\kappa = 1$  to compute the poling periods since this results in the strongest nonlinear interaction and poling periods are not limited by fabrication techniques.

### III. MODAL ENTANGLEMENT IN 1-D PLANAR WAVEGUIDES

We now consider the generation of entangled photons via nondegenerate SPDC in a 1-D planar waveguide. The structure comprises a dielectric slab of thickness  $h$  and refractive index  $n_1$  embedded in dielectric media with lower refractive index  $n_2$ , as illustrated in Fig. 1. The transverse profile of mode  $m_q$  inside the slab is [19]

$$u_{m_q,\sigma_q}(\omega_q, y, z) \propto \begin{cases} \cos(k_{m_q,\sigma_q}^{(z)}(\omega_q) z), & m_q = \text{even} \\ \sin(k_{m_q,\sigma_q}^{(z)}(\omega_q) z), & m_q = \text{odd}, \end{cases} \quad (11)$$

while outside the slab it is

$$u_{m_q,\sigma_q}(\omega_q, y, z) \propto \exp(-\gamma_{m_q,\sigma_q}(\omega_q) z), \quad (12)$$

where  $k_{m_q,\sigma_q}^{(z)} = (k_{m_q,\sigma_q}^2 - \beta_{m_q,\sigma_q}^2)^{1/2}$  is the  $z$ -component of the wavevector  $k_{m_q,\sigma_q} = n_1\omega_q/c$ ,  $\gamma_{m_q,\sigma_q} = (\beta_{m_q,\sigma_q}^2 - \tilde{k}_{m_q,\sigma_q}^2)^{1/2}$ ,  $\tilde{k}_{m_q,\sigma_q} = n_2\omega_q/c$ , and  $c$  is the velocity of light in free space. Note that both  $n_1$  and  $n_2$  are frequency-dependent.

Within the slab, the mode transverse profiles are either even or odd functions. The propagation constants of the

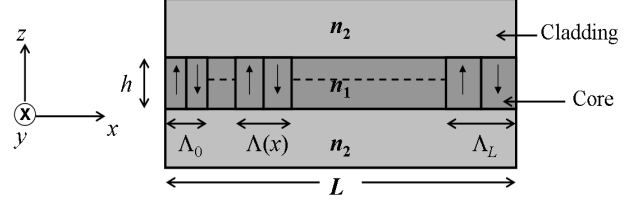


FIG. 1: Sketch of a 1-D planar waveguide. The waveguide is a slab of dielectric medium of thickness  $h$  with a uniform refractive index  $n_1$  surrounded by media of lower refractive index  $n_2$ . The inner medium and the outer media are known as the *core* and *cladding*, respectively. The nonlinear coefficient of the core is poled with a period  $\Lambda(x)$ ; arrows indicate the poling direction. The poling periods at  $x = 0$  and  $x = L$  are denoted  $\Lambda_0$  and  $\Lambda_L$ , respectively.

modes can be determined using the dispersion relation for the planar waveguide. For the TE wave (*o*-polarization),

$$\tan^2\left[\frac{h}{2}\sqrt{k_{m_q,\sigma_q}^2 - \beta_{m_q,\sigma_q}^2} - \frac{m_q\pi}{2}\right] = \frac{\beta_{m_q,\sigma_q}^2 - k_{m_q,\sigma_q}^2}{\tilde{k}_{m_q,\sigma_q}^2 - \beta_{m_q,\sigma_q}^2}, \quad (13)$$

whereas for the TM wave (*e*-polarization), the RHS of the above equation must be multiplied by  $n_1^2/n_2^2$ .

Substituting Eq. (11) into Eqs. (4) and (5), we can determine the functions  $\Phi_{\mathbf{m},\sigma}(\omega_s)$ , which in turn determine the quantum state set forth in Eq. (3). We consider a two-mode waveguide for which the fundamental mode ( $m_q = 0$ ) is even and the next mode ( $m_q = 1$ ) is odd. If the down-converted photons have different spatial parity, the pump mode must be odd so that the spatial overlap integral in Eq. (5), which determines  $A_{\mathbf{m},\sigma}(\omega_s)$  and thence  $\Phi_{\mathbf{m},\sigma}(\omega_s)$ , does not vanish.

We seek to generate an entangled state of the form

$$|\Psi\rangle \sim \int d\omega_s [\Phi_{0,1,\sigma}(\omega_s) |\omega_s, 0, \sigma_s\rangle |\omega_i, 1, \sigma_i\rangle + \Phi_{1,0,\sigma}(\omega_s) |\omega_s, 1, \sigma_s\rangle |\omega_i, 0, \sigma_i\rangle], \quad (14)$$

i.e., if the signal is in the even mode, the idler must be in the odd mode, and vice versa. This requires that the phase-matching condition be satisfied for each of these two possibilities. For a fixed geometry and material parameters, we find a single poling period  $\Lambda_0$  of the nonlinear coefficient at which these conditions,  $\Delta\beta_{0,1,\sigma}(\omega_s) = 2\pi/\Lambda_0$  and  $\Delta\beta_{1,0,\sigma}(\omega_s) = 2\pi/\Lambda_0$ , are simultaneously met. We achieve this by plotting the poling period  $\Lambda_0$  as a function of the signal frequency  $\omega_s$ , or as a function of the signal wavelength  $\lambda_s$ , for each of these two conditions, and search for intersections. The example shown in Fig. 2 reveals that this may occur at a single frequency or, when the two curves are tangential, over a broad spectral band. Once the poling period is selected and fixed, we determine if the spectral functions  $\Phi_{0,1,\sigma}(\omega_s)$  and  $\Phi_{1,0,\sigma}(\omega_s)$  overlap, i.e., have some com-

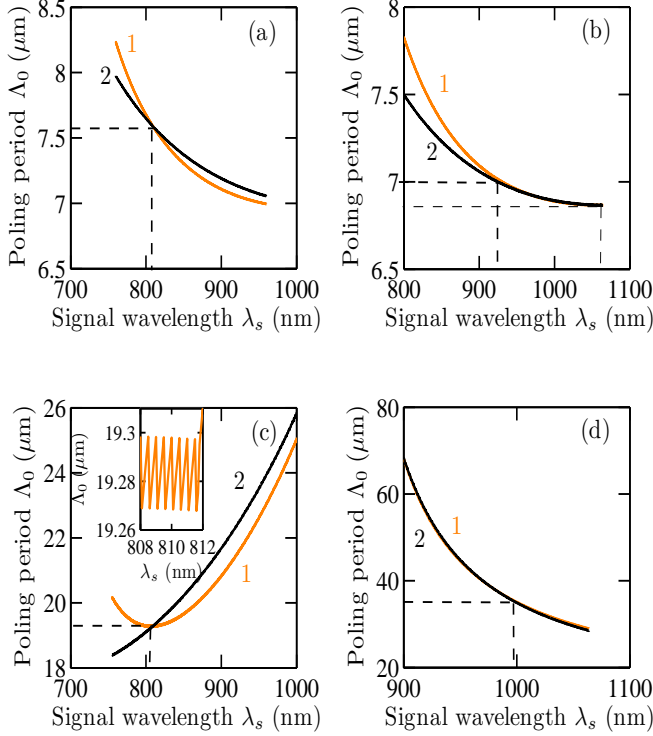


FIG. 2: (Color online). Values of the poling period  $\Lambda_0$  required to satisfy quasi-phase matching as a function of the signal wavelength  $\lambda_s$ , for four values of the waveguide thickness  $h$ . Calculations are presented for a KTP planar waveguide with  $\Delta = 0.05$  pumped by a laser whose wavelength is  $\lambda_p = 532$  nm and whose modal structure coincides with  $m_p = 1$ . The core refractive indexes are determined using the Sellmeier equations for KTP. The orange (black) curves represent condition 1 (2), namely that the signal (idler) mode number  $m_s$  ( $m_i$ ) is 0 and that the idler (signal) mode number  $m_i$  ( $m_s$ ) is 1. Dashed lines indicate intersection points or ranges. (a) Type-0 ( $e, e, e$ ) with waveguide thickness  $h = 1.625 \mu\text{m}$ . (b) Type-0 ( $e, e, e$ ) with  $h = 1.49 \mu\text{m}$ . (c) Type-II ( $o, e, o$ ) with  $h = 1.617 \mu\text{m}$ . The inset shows the behavior of the poling period for condition 1 near the intersection point. (d) Type-II ( $e, o, o$ ) with  $h = 1.56 \mu\text{m}$ .

mon spectral band. If they do, then the two-photon state exhibits entanglement.

**Example.** A laser source with wavelength  $\lambda_p = 532$  nm and in mode  $m_p = 1$ , is used to pump a 1-D periodically poled KTP waveguide with fractional refractive index change  $\Delta \approx 1 - n_2/n_1 = 0.05$ . The core refractive indexes along the  $y$  and  $z$  axes are given by the KTP Sellmeier equations [20]

$$\begin{aligned} n_{1,(y)}^2(\lambda) &= 3.45018 + \frac{0.04341}{\lambda^2 - 0.04597} + \frac{16.98825}{\lambda^2 - 39.43799}, \\ n_{1,(z)}^2(\lambda) &= 4.59423 + \frac{0.06206}{\lambda^2 - 0.04763} + \frac{110.80672}{\lambda^2 - 86.12171}, \end{aligned} \quad (15)$$

where  $\lambda$  is the wavelength expressed in  $\mu\text{m}$ .

The curves in Fig. 2 represent uniform poling-period

values satisfying the quasi-phase-matching conditions versus the signal wavelength  $\lambda_s$ , for four different values of the waveguide thickness  $h$ . The orange (black) curves represent condition 1 (2), namely that the signal (idler) mode number is 0 and the idler (signal) mode number is 1. In panels (a) and (b), the interactions are Type-0 ( $e, e, e$ ), with  $|d_{\text{eff}}| = |d_{33}| = 16.9$  pm/V [21]. The interactions in panels (c) and (d) are Type-II ( $o, e, o$ ) and Type-II ( $e, o, o$ ), respectively, with  $|d_{\text{eff}}| = |d_{24}| = 3.64$  pm/V. The notation  $(\cdot, \cdot, \cdot)$  indicates, in consecutive order, the polarization of the down-converted photon whose frequency lies above the degenerate frequency, the down-converted photon whose frequency lies below the degenerate frequency, and the pump photon.

These plots reveal that the two curves can intersect at a single frequency, as in panels (a) and (c) or, alternatively, they can coincide over a broad range of frequencies, as in panels (b) and (d). Modal entanglement can be obtained at any intersection point since the two quasi-phase-matching conditions are simultaneously satisfied for the unique poling period determined by the point of intersection. In panels (a) and (c),  $h$  has been chosen such that the intersection point between the curves occurs near  $\lambda_s = 810$  nm so that the down-converted photon with the longer wavelength lies in the telecommunications window near 1550 nm. In panels (b) and (d),  $h$  has been chosen such that the two curves are tangential over a broad range of wavelengths.

We now proceed to study the spectral characteristics for the four structures examined in Fig. 2. The fixed poling periods (spatial frequencies) established for panels (a) and (c) in Fig. 2 are used for calculating the spectra presented in panels (a) and (c) in Fig. 3. Similarly, the range of spatial frequencies where the curves overlap in Figs. 2(b) and (d) establish the linearly chirped spatial frequencies used for the calculations displayed in Figs. 3(b) and (d). In all cases, we have chosen a structure of length  $L = 25$  mm.

The output spectra for the two conditions represented by the quantities  $|\Phi_{0,1,\sigma}(\omega_s)|^2$  and  $|\Phi_{1,0,\sigma}(\omega_s)|^2$  are shown in Fig. 3, normalized to the maximum of their peak values. It suffices to plot these quantities solely for signal frequencies above the degenerate frequency  $\omega_p/2$  since

$$\Phi_{0,1,\sigma_i,\sigma_s}(-\omega_s) = \Phi_{1,0,\sigma_s,\sigma_i}(\omega_s). \quad (16)$$

This relation holds by virtue of the definitions of  $A_{\mathbf{m},\sigma}(\omega_s)$  and  $\Delta\beta_{\mathbf{m},\sigma}(\omega_s)$ . Modal entanglement can be achieved over the overlapping regions of the two spectra, as illustrated in Fig. 3. Linearly chirped poling leads to a broadband spectrum by virtue of the continuum of its Fourier domain, so that multiple nonlinear interactions can simultaneously be satisfied [22, 23]. There is, however, a tradeoff between spectral breadth and photon flux density.

The astute reader will have noticed that we have excluded Type-I interactions from our considerations. This is because the down-converted photons have the same

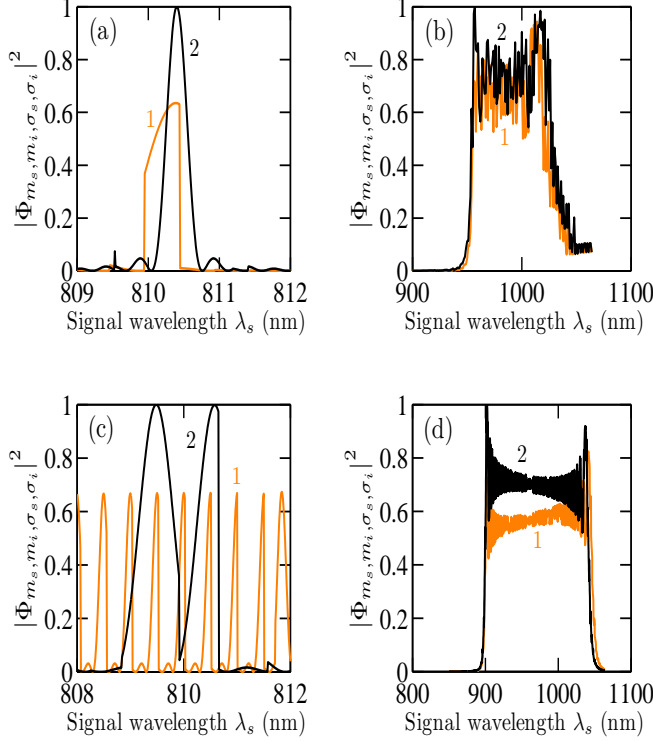


FIG. 3: (Color online). Normalized output spectra  $|\Phi_{\mathbf{m}, \sigma}(\omega_s)|^2 = |\Phi_{m_s, m_i, \sigma_s, \sigma_i}(\omega_s)|^2$  as a function of the signal wavelength  $\lambda_s$ , for the four entanglement conditions shown in Fig. 2. Panels (a) and (b) display modal/spectral entanglement regimes whereas panels (c) and (d) display modal/spectral entanglement and modal/polarization entanglement regimes. The orange (black) curves represent condition 1 (2), namely that the signal (idler) mode number  $m_s$  ( $m_i$ ) is 0 and that the idler (signal) mode number  $m_i$  ( $m_s$ ) is 1. The waveguide length  $L$  is 25 mm. (a) Type-0 ( $e, e, e$ ), uniform poling with  $\Lambda_0 = 7.5816 \mu\text{m}$ . (b) Type-0 ( $e, e, e$ ), linearly chirped poling with  $\Lambda_0 = 6.87 \mu\text{m}$  and  $\Lambda_L = 6.95 \mu\text{m}$ . (c) Type-II ( $o, e, o$ ), uniform poling with  $\Lambda_0 = 19.298 \mu\text{m}$ . The multiple resonances that appear in condition 1 result from the rippled behavior of the poling period near the intersection point, as illustrated in the inset of Fig. 2(c). (d) Type-II ( $e, o, o$ ), linearly chirped poling with  $\Lambda_0 = 30 \mu\text{m}$  and  $\Lambda_L = 70 \mu\text{m}$ .

polarizations as those in Type-0, but Type-I suffers from lower efficiency. The photon flux from a Type-0 interaction is also expected to be greater than that from a Type-II interaction since the former exploits the strongest component of the second-order nonlinear tensor.

#### IV. MODAL ENTANGLEMENT IN 2-D CIRCULAR WAVEGUIDES (SILICA FIBERS)

Although silica is a centrosymmetric material, second-order nonlinearities of  $\sim 1 \text{ pm/V}$  have been observed in poled silicate fibers, see Fig. 4 [24–27]. The presence of a second-order nonlinearity in this centrosymmetric ma-

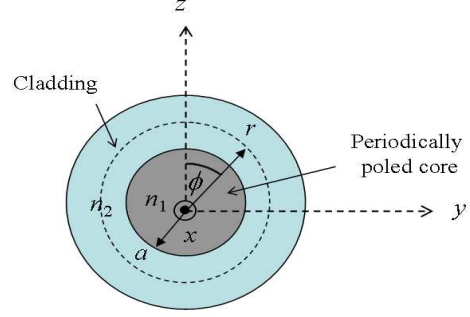


FIG. 4: Sketch of the cross-section of a 2-D circular waveguide. The waveguide is made up of a cylindrical rod of dielectric medium with radius  $a$  and uniform refractive index  $n_1$  surrounded by a medium of lower refractive index  $n_2$ . The inner and the outer media are called the *core* and the *cladding*, respectively. The core is periodically poled in the  $x$  direction.

terial appears to stem from the intrinsic third-order nonlinear susceptibility of the glass and the built-in electric field arising from the displacement of charge species created during the poling process. Although the effective nonlinear coefficient  $|d_{\text{eff}}|$  in silica fiber is substantially smaller than that for many second-order nonlinear materials (e.g.,  $\text{LiNbO}_3$  and  $\text{KTP}$ ), silica fibers are nonetheless of interest because they can be fabricated in very long lengths. Second-order interactions in poled glass fibers can be treated using the same techniques as those developed for QPM structures.

In comparison with 1-D planar waveguides, which carry the index  $m_q$ , each confined mode of a wave  $q$  in a 2-D circular waveguide is marked by an additional index,  $l_q$ . Based on the geometry of the circular waveguide, cylindrical coordinates are a natural choice for describing the transverse mode profile [19]:

$$u_{l_q m_q}(\omega_q, r, \phi) = \begin{cases} J_{l_q}(k_{l_q m_q}^{(T)} r) \exp(j l_q \phi) & r \leq a \\ K_{l_q}(\gamma_{l_q m_q} r) \exp(j l_q \phi) & r > a. \end{cases} \quad (17)$$

Here  $r$  and  $\phi$  are the radial and azimuthal coordinates, respectively;  $l_q = 0, \pm 1, \pm 2, \dots$ ;  $m_q = 1, 2, 3, \dots$ ;  $J_{l_q}(\cdot)$  is the Bessel function of the first kind of order  $l_q$ ;  $K_{l_q}(\cdot)$  is the modified Bessel function of the second kind of order  $l_q$ ;  $k_{l_q m_q}^{(T)} = [(n_1 \omega_q / c)^2 - \beta_{l_q m_q}^2]^{1/2}$ ;  $\gamma_{l_q m_q} = [\beta_{l_q m_q}^2 - (n_2 \omega_q / c)^2]^{1/2}$ ; the superscript  $(T)$  represents the transverse component of the wavevector  $k_{l_q m_q}$ ;  $a$  is the radius of the fiber core; and  $n_1$  and  $n_2$  are the refractive indexes of the core and cladding, respectively (they are frequency-dependent).

The total number of modes  $N_q$  is determined by the value of the fiber parameter  $V_q = (\omega_q a / c)(n_1^2 - n_2^2)^{1/2}$ . If, for example,  $2.405 < V_q < 3.83$ , then  $l_q = 0, \pm 1$  and  $m_q = 1$ , so that  $N_q = 3$ . For each value of  $l_q$ , the mode propagation constants  $\beta_{l_q m_q}$  can be determined by solv-

ing the fiber characteristic equation for  $k^{(T)}$  [19],

$$X \frac{J_{l_q \pm 1}(X)}{J_{l_q}(X)} = \pm Y \frac{K_{l_q \pm 1}(Y)}{K_{l_q}(Y)}, \quad (18)$$

where  $X = k^{(T)}a$  and  $Y = (V_q^2 - X^2)^{1/2}$ . The values of  $k^{(T)}$  that satisfy the characteristic equation are  $k_{l_q m_q}^{(T)}$ . Using the definitions provided above, we can then determine  $\beta_{l_q m_q}$ . The subscript  $\sigma$  has been eliminated in this section since glass fiber is an isotropic material and the characteristic equation is polarization-independent.

In 2-D circular waveguides, the two-photon quantum state is

$$|\Psi\rangle \sim \int d\omega_s \sum_{\mathbf{l}\mathbf{m}} \Phi_{\mathbf{l}\mathbf{m}}(\omega_s) |\omega_s, l_s m_s\rangle |\omega_i, l_i m_i\rangle, \quad (19)$$

where  $\mathbf{l}\mathbf{m} = (l_s m_s, l_i m_i)$ ,  $\Phi_{\mathbf{l}\mathbf{m}}(\omega_s)$  can be determined from Eq. (4) and the amplitude  $A_{\mathbf{l}\mathbf{m}}(\omega_s)$  in cylindrical coordinates is given by

$$A_{\mathbf{l}\mathbf{m}}(\omega_s) = \int_0^a dr \int_0^{2\pi} d\phi r \prod_{q=p,s,i} u_{l_q m_q}(\omega_q, r, \phi). \quad (20)$$

Substituting Eq. (17) into Eq. (20) and performing the azimuthal integration leads to  $\delta(l_p + l_s + l_i)$ , which can be viewed as a limitation on the transverse profiles of the interacting modes (similar to that for planar waveguides).

Consider nondegenerate SPDC in an optical fiber with  $2.405 < V_q < 3.83$ . We seek to generate photon pairs with the following entangled state:

$$|\Psi\rangle \sim \int d\omega_s [\Phi_{01,11}(\omega_s) |\omega_s, 01\rangle |\omega_i, 11\rangle + \Phi_{11,01}(\omega_s) |\omega_s, 11\rangle |\omega_i, 01\rangle], \quad (21)$$

signifying that if the signal is in the fundamental mode ( $l_s m_s = 01$ ), then the idler will be in the first mode ( $l_i m_i = 11$ ), and vice versa. To have nonvanishing  $A_{\mathbf{l}\mathbf{m}}(\omega_s)$  or  $\Phi_{\mathbf{l}\mathbf{m}}(\omega_s)$ , the pump mode index  $l_p m_p$  must be  $(-11)$ .

**Example.** A pump source, with wavelength  $\lambda_p = 532$  nm and in mode  $l_p m_p = -11$ , is incident on an optical glass poled fiber with fractional refractive-index change  $\Delta = 0.01$ . The core refractive index is computed using the Sellmeier equation for fused silica [19]

$$n_1^2(\lambda) = 1 + \frac{0.6962\lambda^2}{\lambda^2 - (0.06840)^2} + \frac{0.4079\lambda^2}{\lambda^2 - (0.1162)^2} + \frac{0.8975\lambda^2}{\lambda^2 - (9.8962)^2}, \quad (22)$$

where  $\lambda$  is the wavelength expressed in  $\mu\text{m}$ . Panels (a) and (b) in Fig. 5 represent the dependence of the uniform poling period on the signal wavelength  $\lambda_s$  required to satisfy quasi-phase matching for the two conditions under consideration, for two different values of the core radius

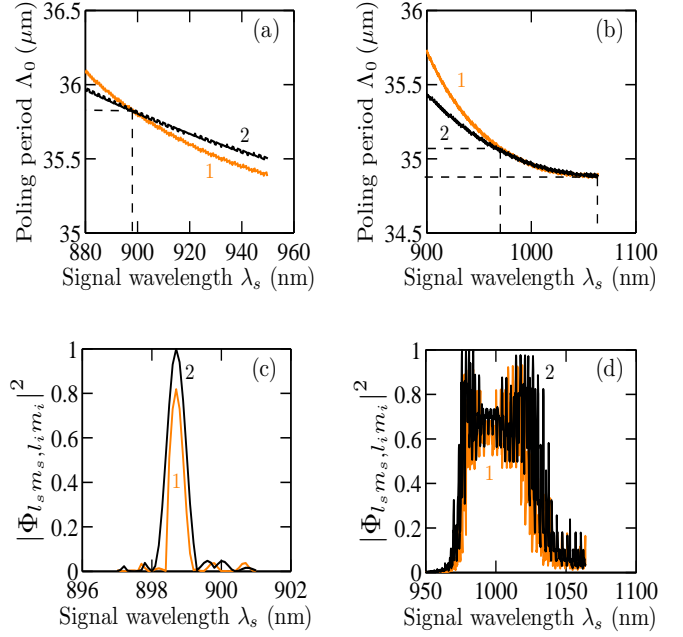


FIG. 5: (Color online). A laser source with wavelength  $\lambda_p = 532$  nm and in mode  $l_p m_p = -11$  is used to pump a poled silica fiber with  $\Delta = 0.01$ . (a) and (b) Poling period versus the signal wavelength  $\lambda_s$ , with core radii  $a = 2.613$  and  $a = 2.52 \mu\text{m}$ , respectively. The orange (black) curve represents condition 1 (2), namely that the signal (idler) mode number  $l_s m_s$  ( $l_i m_i$ ) is 01 and the idler (signal) mode number  $l_i m_i$  ( $l_s m_s$ ) is 11. Dashed lines show the intersection point or region. (c) and (d) These panels display modal/spectral entanglement regimes. Normalized output spectra  $|\Phi_{01,11}(\omega_s)|^2$  and  $|\Phi_{11,01}(\omega_s)|^2$  for the structures displayed in (a) and (b), respectively, with  $L = 20$  cm. The poling period of the nonlinear coefficient is uniform in (c) with  $\Lambda_0 = 35.813 \mu\text{m}$ , and is linearly chirped in (d) with  $\Lambda_0 = 34.9 \mu\text{m}$  and  $\Lambda_L = 35.05 \mu\text{m}$ .

*a.* The curves can either intersect at a single frequency or they can coincide over a broad range of frequencies [in analogy with the results for the 1-D planar waveguide; see Figs. 2(a) and (b)]. Modal entanglement can be achieved where the curves intersect. The core radius  $a$  for panel (a) has been chosen such that the intersection occurs at  $\lambda_s = 900$  nm, placing the down-converted photon with the longer wavelength in the telecommunications window near 1300 nm. In panel (b),  $a$  has been selected such that the two curves are tangential over a broad band of frequencies. Panels (c) and (d) in Fig. 5 display the normalized output spectra  $|\Phi_{01,11}(\omega_s)|^2$  and  $|\Phi_{11,01}(\omega_s)|^2$  for fibers of length  $L = 20$  cm. The poling periods of the fibers used in (c) and (d) are determined from the results obtained in (a) and (b), respectively. Modal entanglement can be achieved in wavelength regions where the spectra overlap.



## V. FEATURES OF MODAL ENTANGLEMENT

In the previous sections, we have demonstrated that it is possible to obtain modal entanglement in 1-D planar and 2-D circular waveguides. In this section, we discuss various features and applications of modal entanglement.

### Combining the advantages of noncollinear and collinear-degenerate interactions in bulk crystals.

A noncollinear configuration is often preferred in bulk crystals because the photon pairs generated by SPDC are easily separated. This process is typically not efficient, however, since the fraction of the photons that are entangled is seriously limited by the intersections between the emission cones. A degenerate-collinear configuration, on the other hand, creates impediments to separating the photon pairs but offers high efficiency by virtue of the total overlap of the emission cones. In a two-mode waveguide with modal entanglement, in contrast, the photon pairs are efficiently generated in the two allowed entangled modes and are thus also readily separated by their mode numbers, i.e., their different transverse-field profiles. This can be implemented by use of a branching waveguide [28].

**Device flexibility and compatibility.** Using uniform or linearly chirped poling, we are able to generate either narrowband or broadband spectral/polarization entanglement, as illustrated in Fig. 3. By replacing the branching waveguide at the device output with a diffraction grating, prism, or polarizing beam splitter (for Type-II), we can obtain binary modal entanglement. The structure can then be used as a source of binary and continuum entanglement that is expected to be useful for applications such as quantum imaging [29–31], quantum cryptography [32], quantum teleportation [33], and quantum information [34]. We note that this waveguide configuration is compatible with integrated optics, which can facilitate its incorporation into a practical system.

**Spectral entanglement** is typically measured via a Hong-Ou-Mandel interferometer (HOM) [35]. An experiment is conducted by sweeping a temporal delay  $\tau$  inserted between the down-converted photons while measuring the coincidence rate of photon counts at a pair of detectors placed at the two output ports of the interferometer. The coincidence rate  $R(\tau)$  is given by

$$R(\tau) = \frac{1}{2} \{R_0 - \text{Re}[R_1(\tau)]\} \quad (23)$$

with

$$\begin{aligned} R_0 &= \int d\omega_s |\Phi_{\mathbf{m},\sigma}(\omega_s)|^2, \\ R_1(\tau) &= \int d\omega_s \{ \Phi_{\mathbf{m},\sigma}(\omega_s) \Phi_{\mathbf{m},\sigma}^*(-\omega_s) \\ &\quad \times \exp[j(\omega_p - 2\omega_s)\tau] \}, \end{aligned} \quad (24)$$

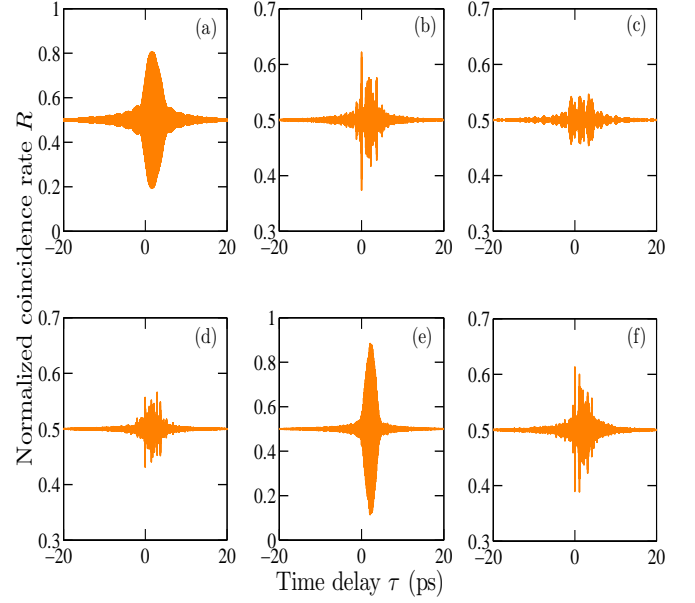


FIG. 6: (Color online). Dependence of the normalized coincidence rate  $R$  on the time delay  $\tau$  between the two photons calculated for a HOM interferometer. (a) 1-D planar waveguide with uniform poling and Type-0 interaction. (b) 1-D planar waveguide with linearly chirped poling and Type-0 interaction. (c) 1-D planar waveguide with uniform poling and Type-II interaction. (d) 1-D planar waveguide with linearly chirped poling and Type-II interaction. (e) 2-D circular waveguide with uniform poling and Type-0 interaction. (f) 2-D circular waveguide with linearly chirped poling and Type-0 interaction. The structure and operational parameters for panels (a), (b), (c), (d), (e), and (f) are the same as those used for Fig. 3(a), (b), (c), (d), and Fig. 5(c) and (d), respectively.

where  $\text{Re}$  denotes the real part and the superscript  $*$  represents the complex conjugate. The integration covers the entire spectrum, so that either  $\Phi_{m_0,m_1,\sigma}(\omega_s)$  or  $\Phi_{m_1,m_0,\sigma}(\omega_s)$  can be used to evaluate the integral, where  $m_0$  and  $m_1$  are the two lowest modes of a waveguide. Again, changing the spatial mode number is equivalent to changing the sign of the frequency, i.e.,  $\Phi_{m_0,m_1,\sigma}(-\omega_s) = \Phi_{m_1,m_0,\sigma}(\omega_s)$ .

The graphs presented in Fig. 6 are the normalized coincidence rate expected for an HOM interferometer for the planar and circular waveguide structures described in Secs. III and IV, respectively. Since the signal and idler are nondegenerate, the familiar dip in the coincidence interferogram is modulated by an oscillatory function. When using the mode numbers for identifying the photons, two different phase-matching conditions are required to obtain spectral or polarization entanglement in waveguides, rather than just a single one for bulk crystals. This distinction arises because of the dependence of the propagation constant on the mode number in a waveguide; in bulk crystals the magnitude of

the wavevector is independent of the direction of propagation. Hence,  $\Delta\tilde{\beta}_{m_0,m_1,\sigma}(\omega_s)$  is not exactly equal to  $\Delta\tilde{\beta}_{m_0,m_1,\sigma}(-\omega_s)$ , so that  $\Phi_{\mathbf{m},\sigma}(\omega_s)$  and  $\Phi_{\mathbf{m},\sigma}^*(-\omega_s)$  do not perfectly overlap in the complex domain. This has several consequences: *i*) The interference pattern shifts about  $\tau = 0$  since  $\Phi_{\mathbf{m},\sigma}(\omega_s)\Phi_{\mathbf{m},\sigma}^*(-\omega_s)$  is not purely real. This effect is illustrated in Fig. 6(a) and (e). *ii*) The visibility, which is defined as  $\tilde{V}(\tau) = (R_{\max} - R_{\min}) / (R_{\max} + R_{\min})$ , where  $R_{\max}$  and  $R_{\min}$  are the maximum and minimum values of the  $R(\tau)$ , respectively, is reduced since  $R_0$  is not precisely equal to  $R_{\min}$ . This is clearly observable in the Type-II curves portrayed in Fig. 6(c) and (d). *iii*) The interference pattern is ragged, as depicted in Fig. 6(b) and (f). However, reducing the device length will result in a cleaner interference pattern, since the imaginary part of  $\Phi_{\mathbf{m},\sigma}(\omega_s)\Phi_{\mathbf{m},\sigma}^*(-\omega_s)$  is proportional to the device length for both uniform and linearly chirped poling.

Using Eqs. (8) and (10), we define the *entanglement length*  $L_e$  as the waveguide length for which the phase of  $\Phi_{\mathbf{m},\sigma}(\omega_s)\Phi_{\mathbf{m},\sigma}^*(-\omega_s)$  is equal to  $\pi$ . For uniform poling, we obtain

$$L_e = \left| \frac{2\pi}{\Delta\tilde{\beta}_{m_0,m_1,\sigma}(\omega_s) - \Delta\tilde{\beta}_{m_0,m_1,\sigma}(-\omega_s)} \right|, \quad (25)$$

whereas for linearly chirped poling, we have

$$L_e = \left| \frac{4\pi^2 (\Lambda_0^{-1} - \Lambda_L^{-1})}{\Delta\tilde{\beta}_{m_0,m_1,\sigma}^2(\omega_s) - \Delta\tilde{\beta}_{m_0,m_1,\sigma}^2(-\omega_s)} \right|. \quad (26)$$

To explicitly illustrate that the character of the interference pattern does depend on the device length, we present plots of the coincidence rate for shorter structures in Fig. 7. The visibility of the interference pattern increases and its “noisiness” decreases.

**Polarization entanglement** is measured by splitting a pair of photons using a nonpolarizing beam splitter and then sending them to two Glan-Thompson analyzers [36]. After passage through analyzers oriented at angles  $\theta_1$  and  $\theta_2$ , the coincidence rate turns out to be

$$R(\theta_1, \tau) = \frac{1}{4} \left( R_0 - \frac{1}{2} \sin^2(2\theta_1) \{R_0 + \text{Re}[R_1(\tau)]\} \right), \quad (27)$$

where  $\theta_1 + \theta_2 = 90^\circ$ ; the angles are measured with respect to the *o*-polarization wave. The visibility of the interference pattern is given by  $\tilde{V}(\tau) = \{R_0 + \text{Re}[R_1(\tau)]\} / \{3R_0 - \text{Re}[R_1(\tau)]\}$ . The dependence of the visibility on temporal delay is displayed in Figs. 8(a) and (b) for structures that support Type-II interactions. The effect of the waveguide length on the visibility is depicted in Fig. 8(c), which displays calculations carried out for a 1-D KTP planar waveguide pumped using an *o*-polarized wave to generate Type-II (*e, o, o*) down-conversion. The nonlinear coefficient is taken to be uniformly poled with a period  $\Lambda_0 = 67.7768 \mu\text{m}$  so

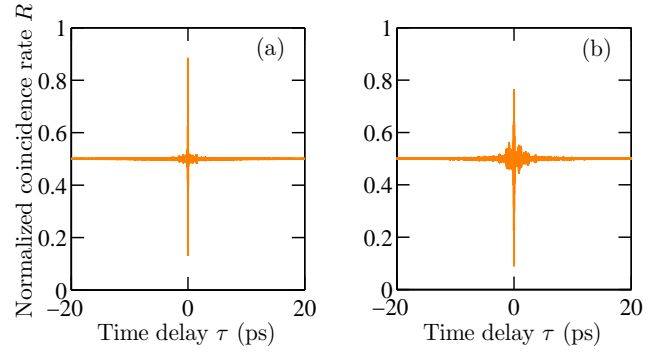


FIG. 7: (Color online). Dependence of the normalized coincidence rate  $R$  on the time delay  $\tau$  between the two photons for a HOM interferometer. (a) 1-D planar waveguide with linearly chirped poling and Type-II interaction. (b) 2-D circular waveguide with linearly chirped poling and Type-0 interaction. The structure and operational parameters for panel (a) are the same as those used for Figs. 3(d) and 6(d) except that  $L = 2 \text{ mm}$  instead of  $25 \text{ mm}$ . The structure and the operational parameters for panel (b) are the same as those used for Figs. 5(d) and 6(f) except that  $L = 20 \text{ mm}$  instead of  $20 \text{ cm}$ .

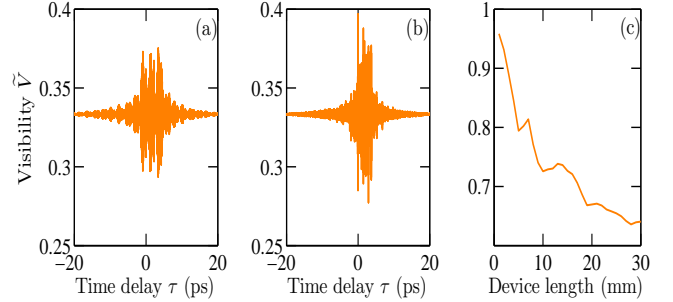


FIG. 8: (Color online). (a) and (b) Dependence of the visibility  $\tilde{V}$  of the interference pattern on the time delay  $\tau$  between the down-converted photons in Type-II interactions for 1-D planar waveguides with uniform and linearly chirped poling, respectively. The structure and operational parameters for panels (a) and (b) are the same as those used for Fig. 3(c) and (d), respectively. (c) Dependence of the visibility  $\tilde{V}$  on the device length  $L$  for a 1-D planar waveguide with uniform poling in a Type-II interaction. The parameters are the same as those used for Fig. 2(d), with a uniform poling period  $\Lambda_0 = 67.7768 \mu\text{m}$

that the wavelength of one of the down-converted photons lies in one of the optical telecommunications windows. The other parameters are the same as those used for Fig. 2(d). The visibility is seen to degrade with increasing waveguide length. Hence, there is a tradeoff between long waveguide length to generate a high flux of photon pairs and short waveguide length to generate a smooth interference pattern with high visibility.



**Modal entanglement** can be considered as an alternative to polarization entanglement. Whereas polarization entanglement is restricted to Type-II interactions, modal entanglement has the merit that it can be generated using any type of nonlinear interaction, including Type-0. Indeed, the down-conversion generation rate in Type-0 is about one order of magnitude higher than that in Type-II, since Type-0 utilizes the strongest component of the second-order nonlinear tensor. Hence, SPDC generated via Type-0 modal entanglement in a waveguide can serve as an efficient source of binary entangled photons.

**An increase in the overall signal-to-noise ratio in an infrared biphoton system** can be achieved by choosing the waveguide dimensions such that one of the photons falls in the visible region while the other lies in the infrared region. This technique can be useful since the visible photon can be efficiently detected with a Si photon-counting detector while the infrared photon is detected with a less efficient InGaAs photon-counting detector. The overall signal-to-noise ratio is increased as a consequence [30, 37].

**Generation of a doubly entangled state via modal entanglement.** Although Type-II is less efficient than Type-0, this configuration can be exploited to generate a doubly entangled state in frequency and polarization [8],

$$|\Psi\rangle \sim (|\omega_s, \omega_i\rangle + |\omega_i, \omega_s\rangle \otimes |\sigma_s, \sigma_i\rangle + |\sigma_i, \sigma_s\rangle). \quad (28)$$

This state can be viewed as a combination of Type-II  $(o, e, o)$  and Type-II  $(e, o, o)$ . The photon pairs can be separated on the basis of their mode number with the help of a branching waveguide. Using Eq. (6), four different nonlinear processes are required to generate the doubly entangled state:

$$|\Psi\rangle \sim \int d\omega_s [\Phi_{0,1,o,e}(\omega_s) |\omega_s, o\rangle_0 |\omega_i, e\rangle_1 + \Phi_{1,0,o,e}(\omega_s) |\omega_i, e\rangle_0 |\omega_s, o\rangle_1 + \Phi_{0,1,e,o}(\omega_s) |\omega_s, e\rangle_0 |\omega_i, o\rangle_1 + \Phi_{1,0,e,o}(\omega_s) |\omega_i, o\rangle_0 |\omega_s, e\rangle_1]. \quad (29)$$

Although it is difficult to satisfy the phase-matching condition for all of these processes using uniform poling, this can be achieved by using linearly chirped poling. The nonlinear coefficient can also be poled in an aperiodic sequence to obtain a narrowband doubly entangled state [38].

In Fig. 9(a), we plot the normalized output spectra  $|\Phi_{m_s, m_i, \sigma_s, \sigma_i}|^2$  when an  $o$ -polarized pump source in mode  $m_p = 1$  at  $\lambda_p = 406$  nm is incident on a 1-D KTP planar waveguide with thickness  $h = 1.1$   $\mu\text{m}$ , length  $L = 25$  mm, and  $\Delta = 0.05$ . The poling period of the nonlinear coefficient is linearly chirped with  $\Lambda_0 = 6.5$   $\mu\text{m}$  and  $\Lambda_L = 7.9$   $\mu\text{m}$ . As illustrated in Fig. 9, the output spectra associated with Type-II  $(o, e, o)$  modal entanglement

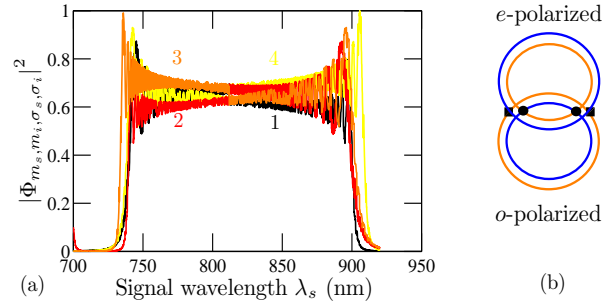


FIG. 9: (Color online). (a) Output spectra of SPDC from a KTP planar waveguide with thickness  $h = 1.1$   $\mu\text{m}$ , length  $L = 25$  mm, and  $\Delta = 0.05$ , using an  $o$ -polarized source in mode  $m_p = 1$  at  $\lambda_p = 406$  nm. The poling period of the nonlinear coefficient is linearly chirped with  $\Lambda_0 = 6.5$   $\mu\text{m}$  and  $\Lambda_L = 7.9$   $\mu\text{m}$ . The black (1) and red (2) curves represent the output spectra associated with Type-II  $(o, e, o)$  modal entanglement, while the orange (3) and yellow (4) curves represent the output spectra associated with Type-II  $(e, o, o)$  modal entanglement. The regions where the four spectra overlap indicate modal/spectral/polarization entanglement. (b) The regions of bulk Type-II  $(o, e, o)$  and Type-II  $(e, o, o)$  polarization entanglement are marked by small black filled circles and squares, respectively. The blue and orange rings represent photons with frequencies above and below the degenerate frequency, respectively.

overlap with the output spectra associated with Type-II  $(e, o, o)$  modal entanglement. The region of overlap between the four spectra (except for the degenerate case) represents the spectral band over which a doubly entangled state can be obtained. It is worthy of note that this state cannot be generated in bulk crystals since four different directions are required, as shown in Fig. 9(b). In waveguides with modal entanglement, however, only two mode numbers are required.

## VI. CONCLUSION

We have investigated nondegenerate spontaneous parametric down-conversion (SPDC) in multimode 1-D planar and 2-D circular waveguides. Using various types of interactions (Type 0 or II), the generated photons can be entangled in the two lowest mode numbers of the waveguide — we refer to this as “modal entanglement.” The inherent phase mismatch in the process is corrected by modulating the nonlinear coefficient with poling periods (spatial frequencies) that are either uniform or linearly chirped. Since the interaction is collinear within the waveguides, modal entanglement can be used in place of directional entanglement to distinguish between the down-converted photons. Spectral or polarization entanglement can therefore be generated with high efficiency and the entangled photons can be readily separated. We find that there is a tradeoff between long

waveguide length to generate a high flux of photon pairs and short waveguide length to generate a smooth interference pattern with high visibility. In Type-0 interactions, frequency can be used as a mode identifier rather than waveguide mode number, offering the possibility of using modal entanglement in place of polarization entanglement, which requires a Type-II interaction. This is a salutary feature since a Type-0 interaction exploits the strongest component of the second-order nonlinear tensor. The technique can be implemented in any of the optical telecommunications windows by controlling the waveguide dimensions. Finally, we have demonstrated that modal entanglement in a Type-II interaction can be used to generate a doubly entangled state in fre-

quency and polarization. Drawing on a Hilbert space of higher dimensions can offer advantages in quantum-communication protocols and quantum computing.

## Acknowledgments

This work was supported by a U.S. Army Research Office (ARO) Multidisciplinary University Research Initiative (MURI) Grant; and by the Bernard M. Gordon Center for Subsurface Sensing and Imaging Systems (CenSSIS), an NSF Engineering Research Center.

- 
- [1] D. N. Klyshko, *Photons and Nonlinear Optics* (Nauka, Moscow, 1980), chaps. 1 and 6. Translation: Gordon and Breach, New York, 1988.
  - [2] B. E. A. Saleh, A. F. Abouraddy, A. V. Sergienko, and M. C. Teich, Phys. Rev. A **62**, 043816 (2000).
  - [3] A. Joobeur, B. E. A. Saleh, and M. C. Teich, Phys. Rev. A **50**, 3349 (1994).
  - [4] A. Joobeur, B. E. A. Saleh, T. S. Larchuk, and M. C. Teich, Phys. Rev. A **53**, 4360 (1996).
  - [5] A. Mair, A. Vaziri, G. Weihs, and A. Zeilinger, Nature **412**, 313 (2001).
  - [6] A. F. Abouraddy, T. Yarnall, B. E. A. Saleh, and M. C. Teich, Phys. Rev. A **75**, 052114 (2007).
  - [7] T. Yarnall, A. F. Abouraddy, B. E. A. Saleh, and M. C. Teich, Phys. Rev. Lett. **99**, 170408 (2007).
  - [8] J. T. Barreiro, N. K. Langford, N. A. Peters, and P. G. Kwiat, Phys. Rev. Lett. **95**, 260501 (2005).
  - [9] M. Halder, S. Tanzilli, H. de Riedmatten, A. Beveratos, H. Zbinden, and N. Gisin, Phys. Rev. A **71**, 042335 (2005).
  - [10] J. G. Rarity and P. R. Tapster, Phys. Rev. Lett. **64**, 2495 (1990).
  - [11] S. P. Walborn, S. Pádua, and C. H. Monken, Phys. Rev. A **71**, 053812 (2005).
  - [12] M. C. Booth, M. Atature, G. DiGiuseppe, B. E. A. Saleh, A. Sergienko, and M. C. Teich, Phys. Rev. A **66**, 023815 (2002).
  - [13] P. G. Kwiat, K. Mattle, H. Weinfurter, A. Zeilinger, A. V. Sergienko, and Y. Shih, Phys. Rev. Lett. **75**, 4337 (1995).
  - [14] T. Yarnall, A. F. Abouraddy, B. E. A. Saleh, and M. C. Teich, Phys. Rev. Lett. **99**, 250502 (2007).
  - [15] C. H. Bennett and P. W. Shor, IEEE Trans. Inform. Theory **44**, 2724 (1998).
  - [16] K. Banaszek, A. B. U'Ren, and I. A. Walmsley, Opt. Lett. **26**, 1367 (2001).
  - [17] A. Eckstein and C. Silberhorn, Opt. Lett. **33**, 1825 (2008).
  - [18] G. Imeshev, M. A. Arbore, M. M. Fejer, A. Galvanauskas, M. Fermann, and D. Harter, J. Opt. Am. Soc. B **17**, 304 (2000).
  - [19] B. E. A. Saleh and M. C. Teich, *Fundamentals of Photonics* (Wiley, Hoboken, NJ, 2007), 2nd ed.
  - [20] K. Kato and E. Takaoka, Appl. Opt. **41**, 5040 (2002).
  - [21] R. L. Sutherland, *Handbook of Nonlinear Optics* (CRC Press, Boca Raton, FL, 2003), 2nd ed.
  - [22] S. Carrasco, J. P. Torres, L. Torner, A. V. Sergienko, B. E. A. Saleh, and M. C. Teich, Opt. Lett. **29**, 2429 (2004).
  - [23] M. B. Nasr, S. Carrasco, B. E. A. Saleh, A. V. Sergienko, M. C. Teich, J. P. Torres, L. Torner, D. S. Hum, and M. M. Fejer, Phys. Rev. Lett. **100**, 183601 (2008).
  - [24] H. Nasu, H. Okamoto, K. Kurachi, J. Matsuoka, K. Kamiya, A. Mito, and H. Hosono, J. Opt. Am. Soc. B **12**, 644 (1995).
  - [25] P. G. Kazansky, P. S. J. Russell, and H. Takebe, J. Lightwave Technol. **15**, 1484 (1997).
  - [26] P. G. Kazansky and V. Pruneri, J. Opt. Am. Soc. B **14**, 3170 (1997).
  - [27] J. Fage-Pedersen, R. Jacobsen, and M. Kristensen, Opt. Express **13**, 8514 (2005).
  - [28] H. Yajima, Appl. Phys. Lett. **22**, 647 (1973).
  - [29] A. F. Abouraddy, B. E. A. Saleh, A. V. Sergienko, and M. C. Teich, Phys. Rev. Lett. **87**, 123602 (2001).
  - [30] A. F. Abouraddy, B. E. A. Saleh, A. V. Sergienko, and M. C. Teich, J. Opt. Am. Soc. B **19**, 1174 (2002).
  - [31] M. B. Nasr, D. P. Goode, N. Nguyen, G. Rong, L. Yang, B. M. Reinhard, B. E. A. Saleh, and M. C. Teich, Opt. Commun. **282**, 1154 (2009).
  - [32] T. Jennewein, C. Simon, G. Weihs, H. Weinfurter, and A. Zeilinger, Phys. Rev. Lett. **84**, 4729 (2000).
  - [33] C. H. Bennett, G. Brassard, C. Crépeau, R. Jozsa, A. Peres, and W. K. Wootters, Phys. Rev. Lett. **70**, 1895 (1993).
  - [34] M. A. Nielsen and I. L. Chuang, *Quantum Computation and Quantum Information* (Cambridge University Press, Cambridge, UK, 2000).
  - [35] C. K. Hong, Z. Y. Ou, and L. Mandel, Phys. Rev. Lett. **59**, 2044 (1987).
  - [36] Y. H. Shih and C. O. Alley, Phys. Rev. Lett. **61**, 2921 (1988).
  - [37] H. G. de Chatellus, A. V. Sergienko, B. E. A. Saleh, M. C. Teich, and G. Di Giuseppe, Opt. Express **14**, 10060 (2006).
  - [38] A. Norton and C. de Sterke, Opt. Express **12**, 841 (2004).